The Vertical Structure of Eddy Heat Transport Simulated by an Eddy-Resolving OGCM

BO YOUNG YIM AND YIGN NOH

Department of Atmospheric Sciences/Global Environmental Laboratory, Yonsei University, Seoul, South Korea

BO QIU

Department of Oceanography, University of Hawaii at Manoa, Honolulu, Hawaii

SUNG HYUP YOU

National Institute of Meteorological Research, Seoul, South Korea

JONG HWAN YOON

Research Institute for Applied Mechanics, Kyushu University, Kasuga, Japan

(Manuscript received 18 February 2009, in final form 16 September 2009)

ABSTRACT

The vertical structure of meridional eddy heat transport (EHT) of the North Pacific was investigated by analyzing the results from an eddy-resolving ocean general circulation model (OGCM) with a horizontal resolution of $^1/_{12}°$, while comparing with previous simulation results and observation data. In particular, the spatial and temporal variation of the effective depth of EHT H_e was investigated, which is defined by the depth integrated EHT (D-EHT) divided by EHT at the surface. It was found that the annual mean value of H_e is proportional to the eddy kinetic energy (EKE) level at the surface in general. However, its seasonal variation is controlled by the mixed layer depth (MLD) in the extratropical ocean (>20°N). Examination of the simulated eddy structures reveals that the temperature associated with mesoscale eddies is radically modified by the surface forcing in the mixed layer, while the velocity field is not, and the consequent enhanced misalignment of temperature and velocity anomalies leads to the radical change of EHT across the seasonal thermocline.

1. Introduction

Various attempts have been made to estimate the heat transport by mesoscale eddies, or eddy heat transport (EHT), which constitutes an important part in the meridional heat transport in the ocean (Wunsch 1999; Roemmich and Gilson 2001).

Estimation of EHT from field observational data has been restricted so far to regional oceans (Bryden 1979; Bryden and Heath 1985; Bryden and Brady 1989; Bower and Hogg 1996; Cronin and Watts 1996; Wunsch 1999; Roemmich and Gilson 2001). Recently, estimation of the global distribution of EHT could be realized by the availability of satellite data of altimetry and sea surface temperature (SST) (Stammer 1998; Stammer et al. 2006; Qiu and Chen 2005). It was found that EHT is significant in the western boundary current and equatorial regions, but is very small in the interior of ocean gyres.

However, information of EHT below the sea surface is not available from satellite data, and an assumption must be introduced for the vertical structure so as to estimate the depth integrated value of EHT (D-EHT). For example, Stammer (1998) assumed that the depth averaged eddy kinetic energy (EKE) over the top 1000 m, which is used to estimate D-EHT by using Fickian diffusion, is approximated as one-tenth of the EKE at the surface. Qiu and Chen (2005) assumed that the effective depth of EHT H_e, which is defined as D-EHT divided by EHT at the surface, is constant. They estimated H_e = 177 m in the subtropical North Pacific by averaging the values of H_e estimated from 102 Argo floats. It is natural,

Corresponding author address: Yign Noh, Department of Atmospheric Sciences/Global Environmental Laboratory, Yonsei University, Seoul, 120-749 South Korea.
E-mail: noh@yonsei.ac.kr

DOI: 10.1175/2009JPO4243.1

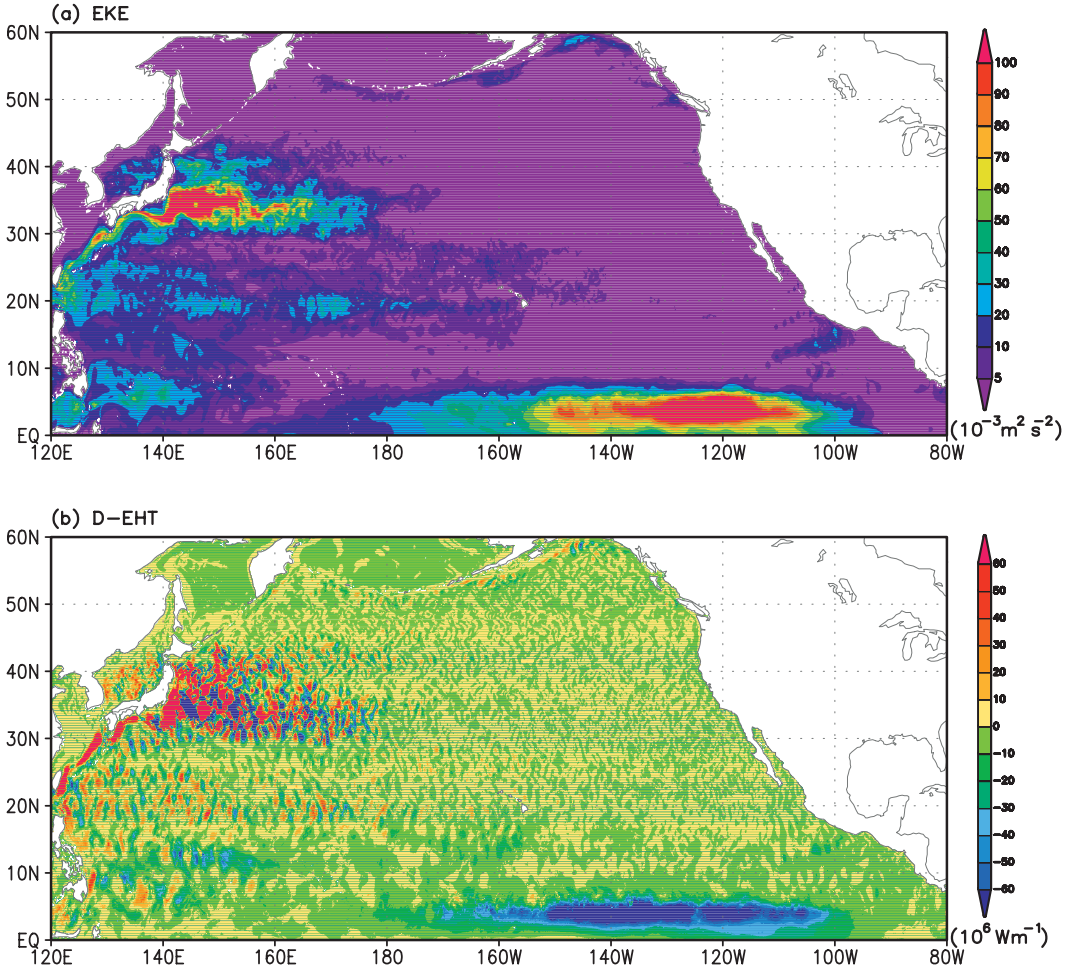

FIG. 1. Distributions in the North Pacific from the OGCM: (a) eddy kinetic energy (EKE) at the surface and (b) depth integrated eddy heat transport (D-EHT).

however, to expect both spatial and temporal variation in H_e.

On the other hand, recent progress in the eddy-resolving ocean general circulation model (OGCM) enables us to estimate D-EHT directly (Jayne and Marotzke 2002; Meijers et al. 2007; Volkov et al. 2008). Using an OGCM with a horizontal resolution of ¼°, Jayne and Marotzke (2002) reproduced the distribution of D-EHT, and compared it with the estimation from satellite data by Stammer (1998). They also showed that the large values for D-EHT in the western boundary currents and the Antarctic Circumpolar Current arise from the meandering of the currents, while they arise from tropical instability waves in the tropical ocean. The horizontal resolution of ¼° may not be sufficient to resolve mesoscale eddies, and the estimation of D-EHT from a higher-resolution OGCM is reported recently: for example, the resolution of ⅛° in Meijers et al. (2007).

No serious effort has yet been made to clarify the vertical structure of EHT from OGCM data. Jayne and Marotzke (2002) calculated EHT in four different depth ranges, and found that EHT is largely confined to the upper 1000 m. Based on the analysis of observation data, Qiu and Chen (2005) suggested that the misalignment between temperature and velocity anomalies, which is necessary for the generation of EHT, is largely confined to the mixed layer depth (MLD).

The clarification of the vertical structure of EHT provides essential information not only for the estimation of D-EHT from satellite data but also for the parameterization of lateral mixing in coarse-resolution OGCMs (Killworth 1998). It also helps us to understand the dynamics of mesoscale eddies and their effect on ocean circulation (Marshall et al. 2002). In this paper, the vertical structure of meridional EHT is investigated by analyzing the results from an eddy-resolving OGCM with a horizontal resolution of 1/12°, and the evaluated

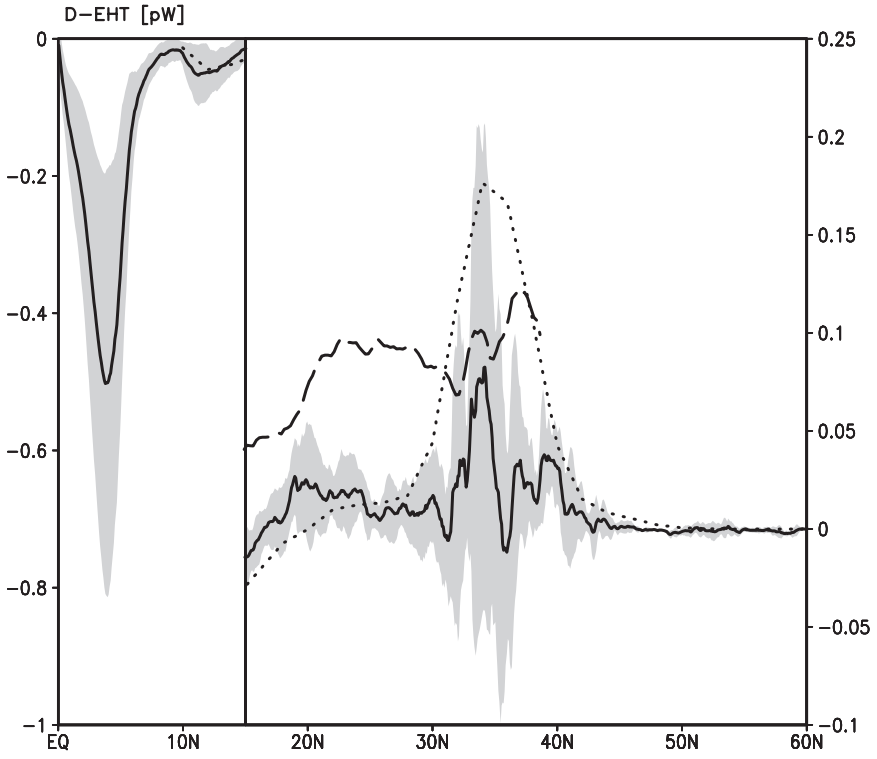

FIG. 2. Zonally integrated D-EHT in the North Pacific (solid line). Dashed and dotted lines denote the estimate from Qiu and Chen (2005) and Stammer et al. (2006), respectively. Shaded areas denote the standard deviation associated with the solid line.

EHT is compared with the previous estimations. Especially the distribution of H_e and its seasonal variation are examined, and its relationship to the MLD and the penetration depth of EKE is investigated. To clarify the effect of the MLD on EHT, the structure of mesoscale eddies is examined along with vertical profiles of various variables. In this paper, EHT always refers to the heat transport in the meridional direction.

2. Model

The OGCM used in this study [Research Institute for Applied Mechanics (RIAM) Ocean Model (RIAMOM)] is a primitive equation general ocean circulation model with a free surface that assumes the Boussinesq and hydrostatic approximations. The model covers the Pacific Ocean from 50°S to 65°N, 95°E to 70°W. The horizontal grid interval is $1/12°$ in both latitudinal and longitudinal directions with 70 vertical levels. Its vertical grid intervals are 10–125 m for the depth 0–2420 m and 200–250 m below 2420 m. Note that the horizontal resolution of the OGCM must be smaller than $1/10°$ to resolve mesoscale eddies globally (Smith et al. 2000). The advection of momentum is treated by the generalized Arakawa scheme (Ishizaki and Motoi 1999), which conserves potential enstrophy as well as kinetic energy. It also uses an improved advection scheme of tracers by Webb et al. (1998) and the biharmonic diffusion for both momentum and tracers. Vertical mixing is parameterized by the Noh scheme, which was shown to reproduce realistic subsurface stratification (Noh and Kim 1999; Noh et al. 2002, 2007). The present OGCM was shown to reproduce realistically not only the mean structure of the ocean, but also the distribution of EKE and its seasonal variation (Noh et al. 2007). The detailed explanation and general performance of the model can be found in You (2005) and Hirose et al. (2007).

The model was integrated from a state of rest with the climatological mean temperature and salinity distribution of WOA94 (Levitus and Boyer 1994; Levitus et al. 1994) and forced by the climatological forcing of monthly mean wind stress and heat flux from the National Centers for Environmental Prediction reanalysis data with regression. The heat flux was given by the combined boundary condition that uses both the climatological flux and a restoring term with a restoring time scale of 30 days, similar to Noh et al. (2002). The sea surface salinity was restored with a restoring time scale of 10 days. All lateral boundaries adjoining the ocean were closed, and temperature and

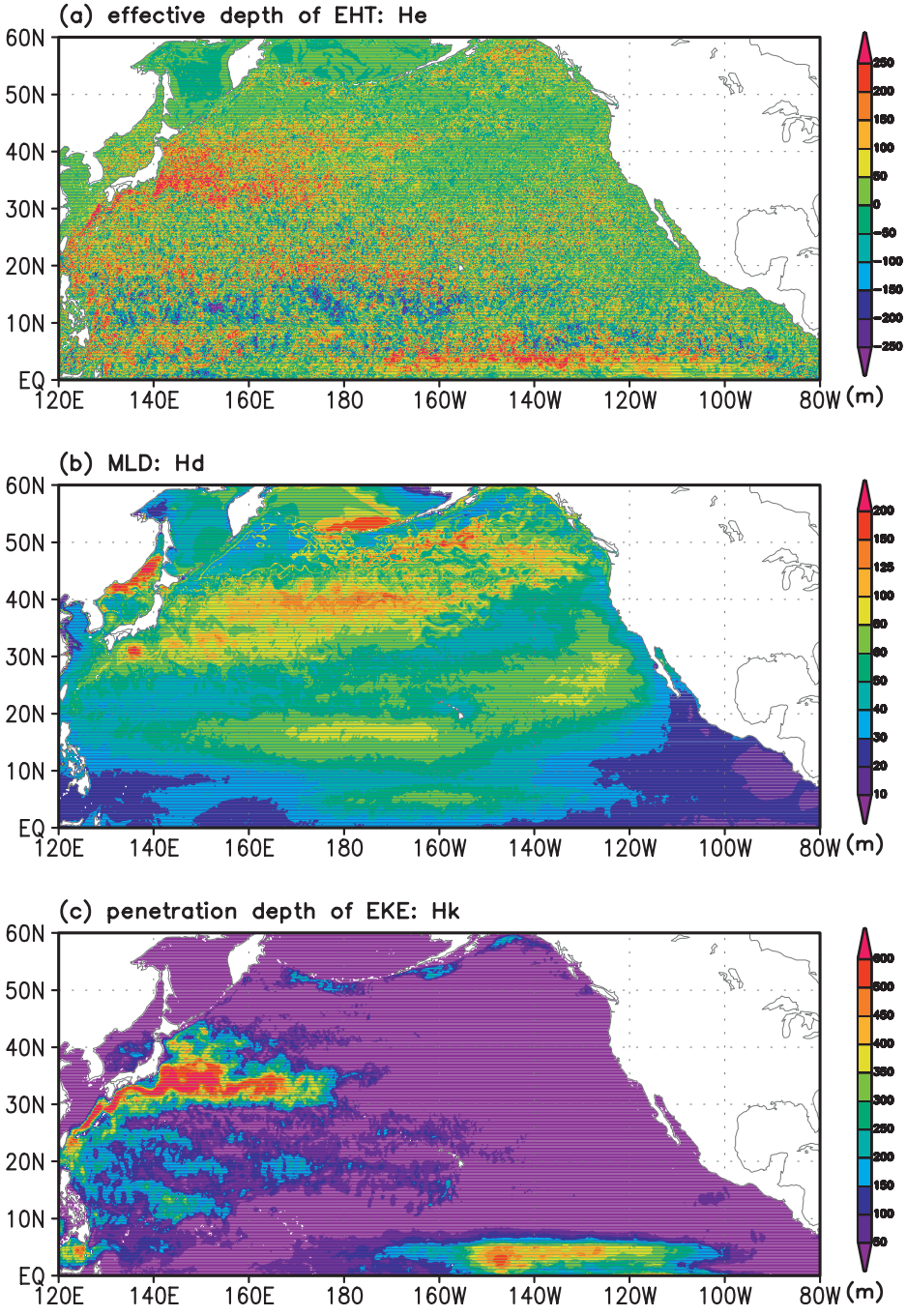

FIG. 3. Distributions in the North Pacific from the OGCM: (a) H_e, (b) H_d, and (c) H_k.

salinity were restored to the climatological value at the boundary.

The model was integrated for 25 years, which is long enough for the upper ocean to reach quasi-equilibrium. Three-dimensional prognostic variables were archived at every model day of the final year and were used for analysis. The OGCM data were analyzed only for the North Pacific (0°–60°N, 120°E–80°W).

3. Results

a. Distributions of EKE and D-EHT

Figure 1 shows the distribution of the annual mean values of EKE at the surface and D-EHT in the North Pacific obtained from the OCGM. Here EKE ($=(\overline{u'u'} + \overline{v'v'})/2$) and D-EHT ($=\rho c_p \int \overline{T'v'}\, dz$) were evaluated by

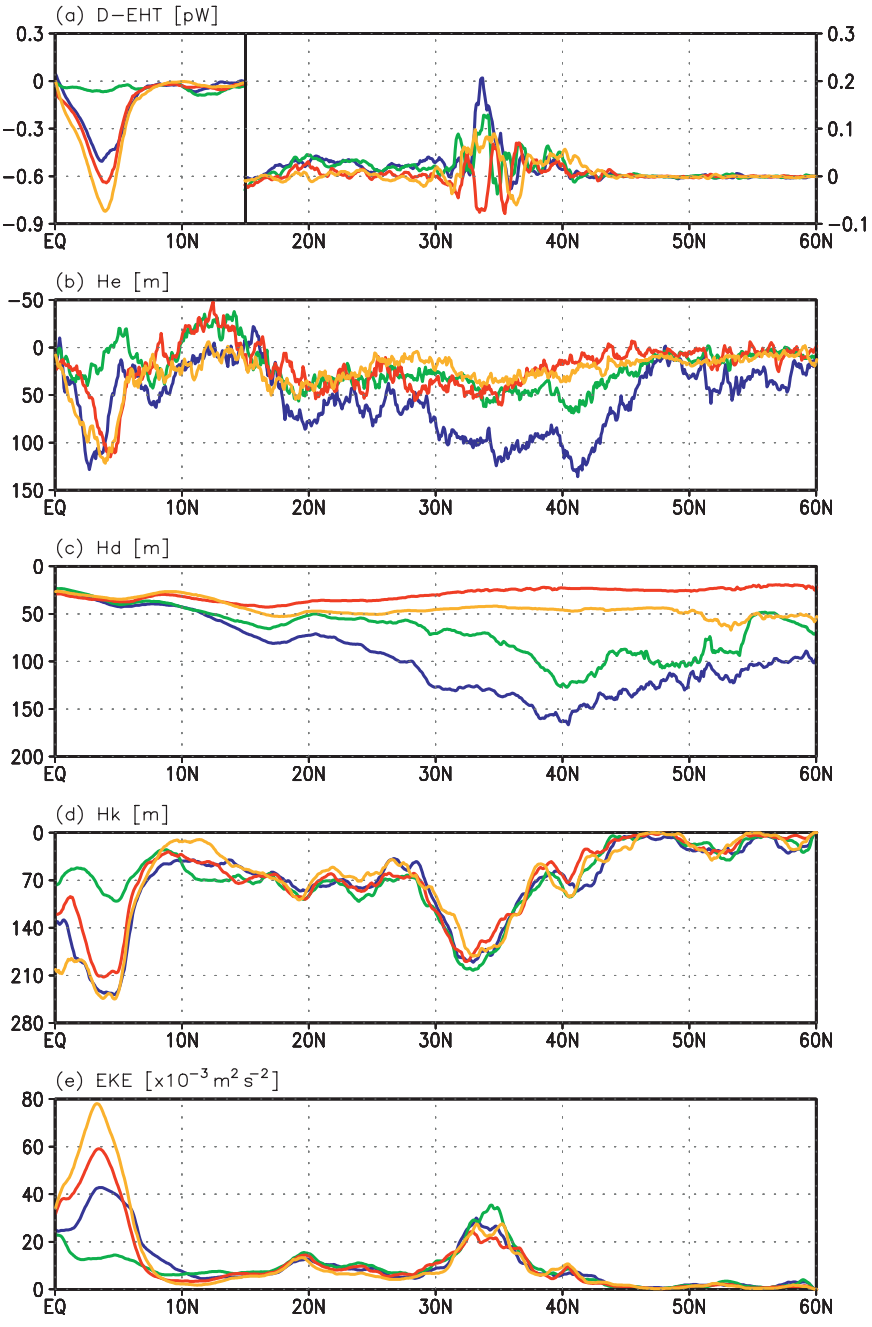

FIG. 4. Meridional variation of the zonally averaged values in the North Pacific from the OGCM at each season [Jan–Mar (JFM): winter (blue); Apr–Jun (AMJ): spring (green); Jul–Sep (JAS): summer (red); and Oct–Dec (OND): fall (yellow)] for (a) D-EHT, (b) H_e, (c) H_d, (d) H_k, and (e) EKE at the surface.

the time average of anomalous velocities and temperature from the monthly mean, where ρ and c_p are the density and heat capacity of water, respectively. Note that the time scales for baroclinic eddies and tropical instability waves are typically less than a month (Qiao and Weisberg 1995; Stammer 1998; Gill 1982).

Analysis of EKE distribution reveals strong EKE near the Kuroshio Extension and the eastern tropical ocean, which is in agreement with previous results from satellite altimetry data and eddy-resolving OGCMs (Stammer 1997; Qiu 1999; Ducet and Le Traon 2001; Maltrud and McClean 2005; see also Noh et al. 2007 for

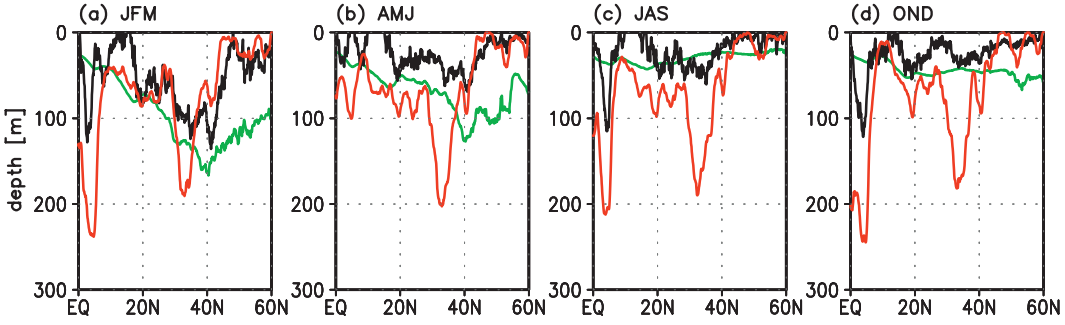

FIG. 5. Comparison of the meridional distribution of the zonally averaged H_e, H_d, and H_k from the OGCM in each season. The black, green, and red lines represent H_e, H_d, and H_k, respectively (JFM, AMJ, JAS, and OND).

the comparison). In the tropical ocean, EKE is due to tropical instability waves, while in the Kuroshio Extension region it arises from the meandering of the currents (Jayne and Marotzke 2002). High EKE levels are also observed along 20°N in the western Pacific, which is due to baroclinic eddies generated along the Subtropical Countercurrent (STCC) (Qiu 1999; Noh et al. 2007).

The distribution of D-EHT is highly correlated with that of EKE, as is also shown in previous results (Stammer 1998; Jayne and Marotzke 2002; Qiu and Chen 2005). Meanwhile, Fig. 1b shows that the D-EHT in the Kuroshio Extension region changes direction alternately along the path of the Kuroshio meandering jet, as observed in previous studies (Wunsch 1999; Jayne and Marotzke 2002; Qiu and Chen 2005). The strong southward D-EHT appears in the eastern part of the zonal band around 5°N in agreement with previous OGCM results (Jayne and Marotzke 2002; Volkov et al. 2008) and field observations (Bryden and Brady 1989; Baturin and Niiler 1997). The existence of the convergence of EHT along the equator was also suggested by previous modeling studies (Philander and Pacanowski 1986).

Figure 2 compares the zonally integrated D-EHT to two estimates from observation data (Qiu and Chen 2005; Stammer et al. 2006). The existence of the D-EHT directional change along the path in the Kuroshio Extension region, as shown in Fig. 1, implies that EHT is often upgradient. Therefore, the estimation based on the assumption of the downgradient EHT with positive eddy diffusivity A_h, such as $\overline{v'T'} = -A_h \partial \overline{T}/\partial y$ by Stammer et al. (2006), has a much larger EHT in the corresponding latitudinal band (~35°N). On the other hand, substantially larger EHT is estimated by Qiu and Chen (2005) in the latitudinal band 20°–30°N. It may be due to the overestimation of H_e in this region, as will be discussed in the next section. The present result is also in general agreement with the previous eddy-resolving OGCM data (Jayne and Marotzke 2002; Volkov et al. 2008), although the model resolution and the method of evaluating EHT are different.

b. Distributions of H_e, H_d, and H_k

To investigate the vertical structure of EHT, the distribution of the annual mean values of H_e is shown along with the distributions of MLD H_d and of the penetration depth of EKE H_k (Fig. 3). Here H_e is calculated from $H_e = \int \overline{v'T'}(z)\, dz / \overline{v'T'}(0)$, as in Qiu and Chen (2005), and H_d is obtained from the criterion $\Delta T = 0.5$°C from the SST (e.g., Monterey and Levitus 1997). Here H_k is defined as the depth at which EKE decreases to 5×10^{-3} m^2 s^{-2}. The estimation of H_k has not been made so far, and the critical level of EKE to determine H_k was chosen rather arbitrarily to distinguish the EKE of the upper and deep ocean most effectively; see, for example, the vertical distribution of EKE shown in Smith et al. (2000).

Large variability is found in the distribution of H_e in Fig. 3a, and its temporal variation is also very large, often with a standard deviation over 100 m. Nonetheless, large values of H_e appear in the regions with large EKE and D-EHT, that is, in the Kuroshio Extension, STCC, and eastern tropical ocean. One can also notice that H_e becomes negative around 10°N. In this region the meridional gradient of the mean temperature $\partial \overline{T}/\partial y$ changes its sign with depth owing to convergence and downwelling in the subtropical gyre. As a result, EHT is directed southward below the surface, while it is directed northward at the surface.

Averaging H_e over the whole domain leads to $H_e =$ 42 m, a substantially smaller value than the value suggested by Qiu and Chen (2005): $H_e = 177$ m. It is probably due to the fact that the Argo data used by them to evaluate H_e was highly concentrated in the Kuroshio Extension region where H_e has larger values.

The OGCM also reproduces H_d values in good agreement with climatological data (Monterey and Levitus 1997; Kara et al. 2003). While it increases with latitude in

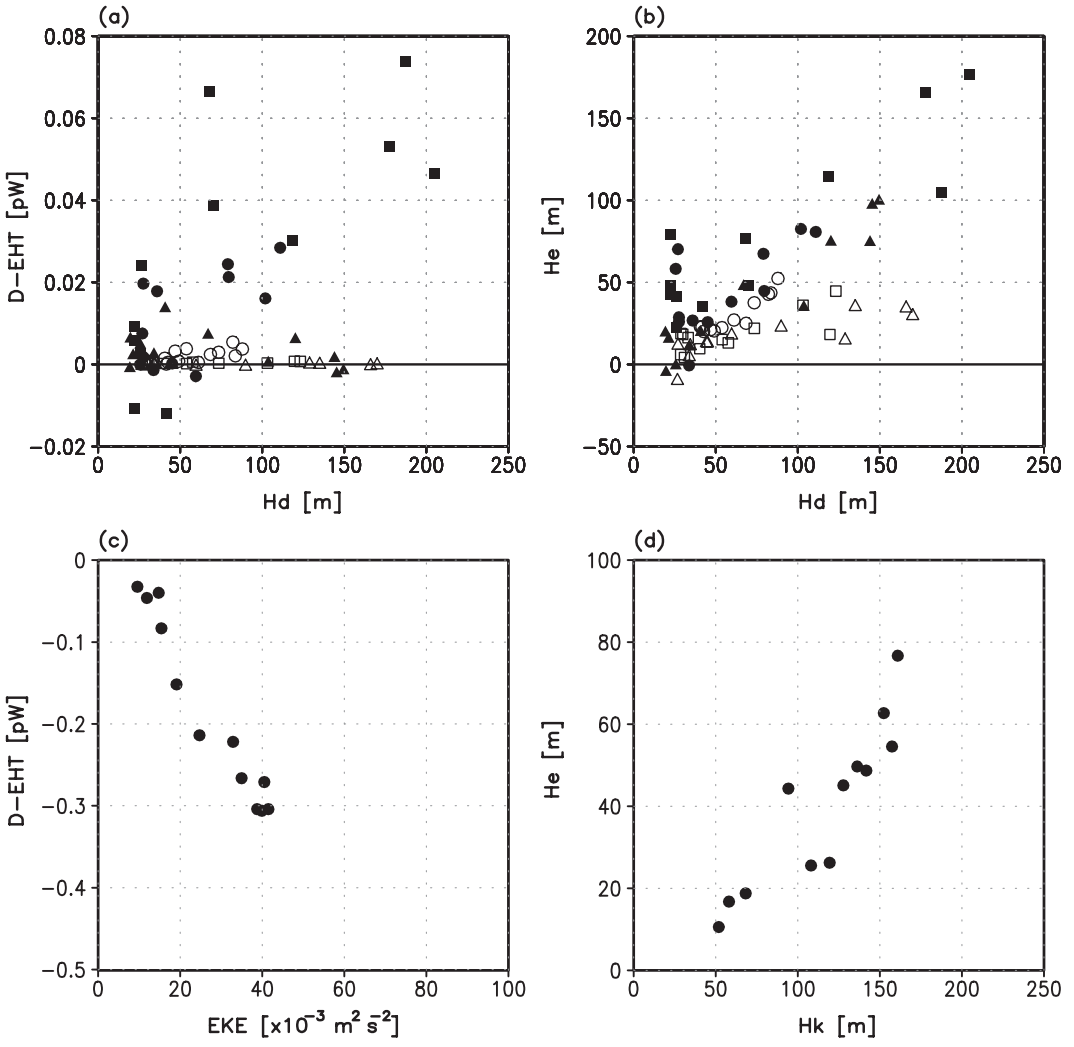

FIG. 6. Scatterplots of monthly mean values for (a) D-EHT vs H_d in the zonal band 20°–50°N [circles, squares, and triangles represent the data from the zonal bands 20°–30°, 30°–40°, and 40°–50°N, respectively, and black and white symbols represent the western (<170°W) and eastern (>170°W) region]; (b) H_e vs H_d in the zonal band 20°–50°N [the symbols are the same as in (a)]; (c) D-EHT vs EKE at the surface in the zonal band 0°–10°N; and (d) H_e vs H_k in the zonal band 0°–10°N.

general, the deeper MLD is found in the Kuroshio Extension region, in the high-latitude ocean, and in the convergence zone of the subtropical gyre near 15°N (Fig. 3b). The local maximum of MLD is also observed along 5°N, which is due to the meridional slope of MLD in association with the North Equatorial Countercurrent (NECC) (see, e.g., Wyrtki and Kilonsky 1984).

It is found that H_k is generally proportional to EKE at the surface, although EKE is less penetrative in the equatorial ocean (Fig. 3c).

One can notice from Fig. 3 that stronger correlation exists between H_e and H_k than between H_e and H_d. Large values of both H_e and H_k are found in the Kuroshio Extension, STCC, and eastern tropical ocean. This suggests that H_e is proportional to H_k—as far as its annual mean value is concerned.

c. *Seasonal variation of H_e, H_d, and H_k*

Although the annual mean value of H_e is found to be largely proportional to H_k, the question still remains as to whether the seasonal variation of EHT at a given location is affected by the strong seasonal variation of MLD. To answer this question, we investigated the seasonal variation of the zonal mean values of D-EHT, H_e, H_d, H_k, and EKE at the surface (Fig. 4). Here the seasonal average is calculated by averaging three-monthly values.

A remarkable feature in Fig. 4 is that the seasonal variations of D-EHT and H_e show different patterns

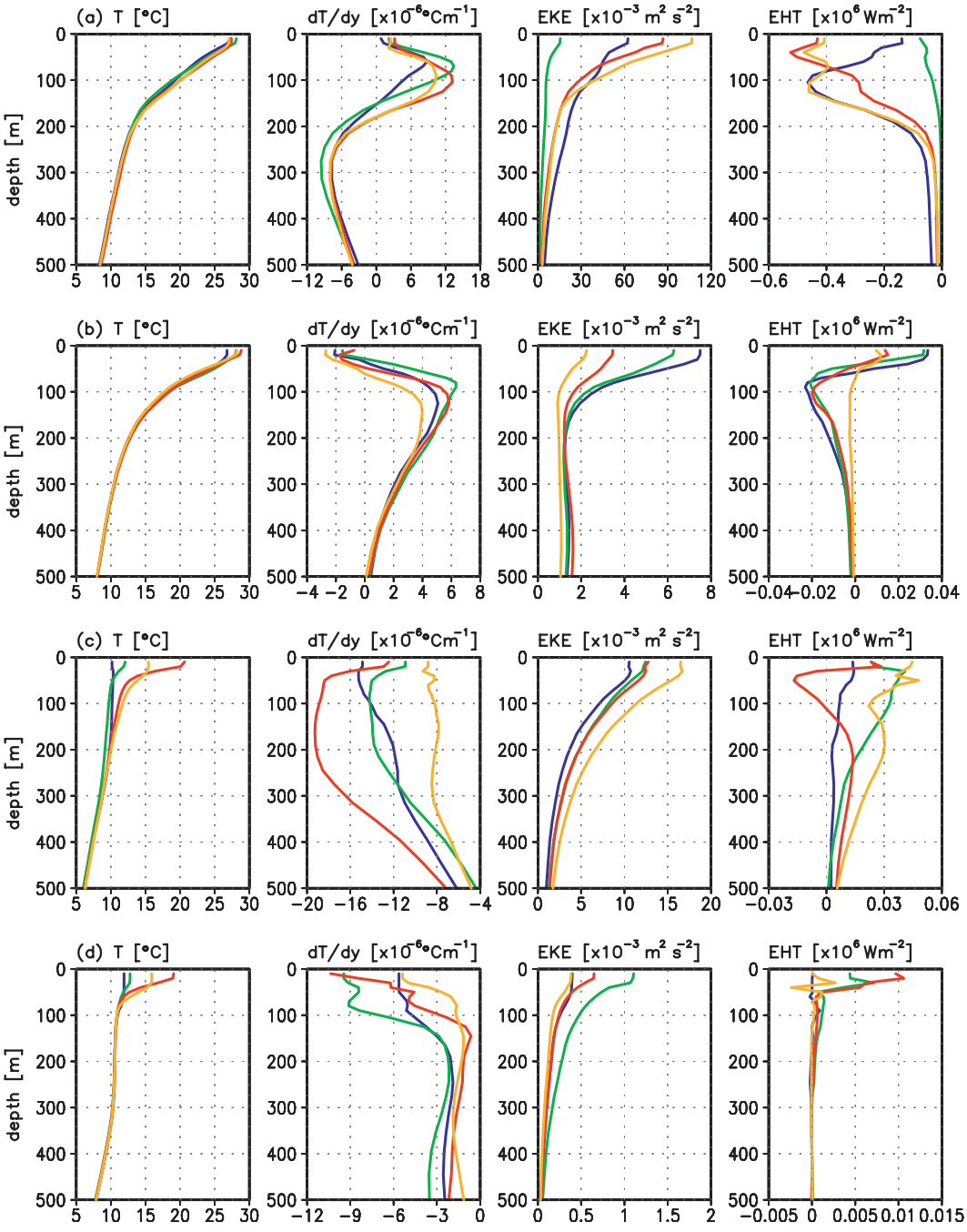

FIG. 7. Vertical profiles of the zonally averaged values of $\overline{T}$, $\partial\overline{T}/\partial y$, EKE, and EHT in JFM: winter (blue), AMJ: spring (green), JAS: summer (red), and OND: fall (yellow) at (a) 4°N east (>170°W), (b) 10°N, (c) 40°N west (<170°W), and (d) 40°N east (>170°W). (Note that horizontal scales are different in all figures.)

depending on whether they are tropical or extratropical. In the extratropical ocean (>20°N) the values of D-EHT and H_e are larger in winter and smaller in summer in accordance with the seasonal variation of H_d. It is also found that D-EHT almost disappears north of 50°N where EKE is very low throughout the zonal band, as shown in Fig. 1. In the tropical ocean (<10°N), however, seasonal variations of D-EHT and H_e are larger in fall and smaller in spring, in accordance with the seasonal variations of EKE and H_k. In particular, the seasonal variation of D-EHT is more closely related to that of EKE, while the seasonal variation of H_e is to that of H_k.

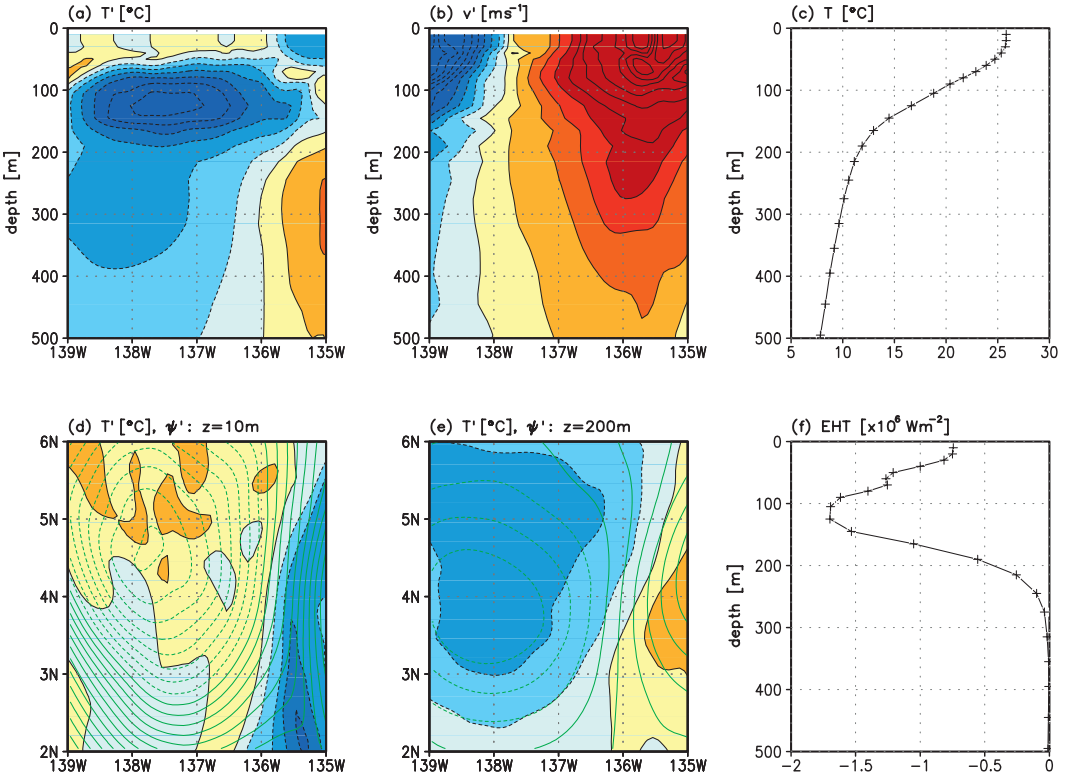

FIG. 8. Eddy structure and EHT in region 4N (2°–6°N, 139°–135°W) on 24 Jan: (a),(b) distributions of T' and v' at the vertical cross section; (c) the vertical profile of mean temperature; (d),(e) distributions of T' (color) and streamfunctions for velocity anomaly ψ' (line) at $z = 10, 200$ m; and (f) the vertical profile of EHT. Contour intervals are 0.5°C, 0.1 m s^{-1}, and 10^4 m^2 s^{-1} for T', v', and ψ'; the blue color represents the area with negative values in all cases.

The seasonal variation of EKE follows that of the intensity of tropical instability waves (Baturin and Niiler 1997; Qiao and Weisberg 1995). The seasonal variations of EKE and H_k in the extratropical ocean are insignificant compared to those in the tropical ocean.

Figure 5 shows the data of Figs. 4b–d replotted to allow for direct comparison between the meridional distribution of the zonally averaged H_e, H_d, and H_k at each season. It illustrates clearly that H_e is proportional to H_k in general but tends to decrease with the decrease of H_d in the extratropical ocean. For example, H_e is deeper in winter than in summer in the extratropical ocean, although H_k remains invariant throughout the season. On the other hand, H_e is always proportional to H_k, independent of H_d in the tropical ocean.

The correlation between these variables can be confirmed in scatterplots of the monthly mean values—that is, D-EHT versus H_d and H_e versus H_d in the zonal band 20°–50°N (Figs. 6a,b), and D-EHT versus EKE and H_e versus H_k in the zonal band 0°–10°N (Figs. 6c,d). In Figs. 6a and 6b different symbols are used to distinguish the eastern and western parts. In the eastern part of the extratropical ocean (Figs. 6a,b) H_e tends to be smaller, and D-EHT is negligible compared to the western part.

d. *Vertical profiles of the zonally averaged $\overline{T}$, $\partial\overline{T}/\partial y$, EKE, and EHT*

To understand the relationship among H_e, H_d, and H_k, we examined vertical profiles of the zonal averages of mean temperature $\overline{T}$, its meridional gradient ($=\partial\overline{T}/\partial y$), EKE, and EHT ($=\rho c_p \overline{T'v'}$) (Fig. 7). Latitudes are chosen to represent the tropical ocean (4°, 10°N; referred to as 4N and 10N, respectively) and the extratropical ocean (40°N). In the case of 4°N, only the eastern part (>170°W) is considered where strong EHT exists. In the case of 40°N, the western part (<170°W) and the eastern part (>170°W) are shown separately to distinguish the influence of the Kuroshio Extension (referred to as 40NW and 40NE, respectively).

The seasonal variation of EHT shows the same trend as that of EKE in the tropical ocean. In 4N, both values of EHT and EKE are very small in spring. They are smaller at the surface but penetrate deeper in winter, as compared to in summer and fall, which makes D-EHT

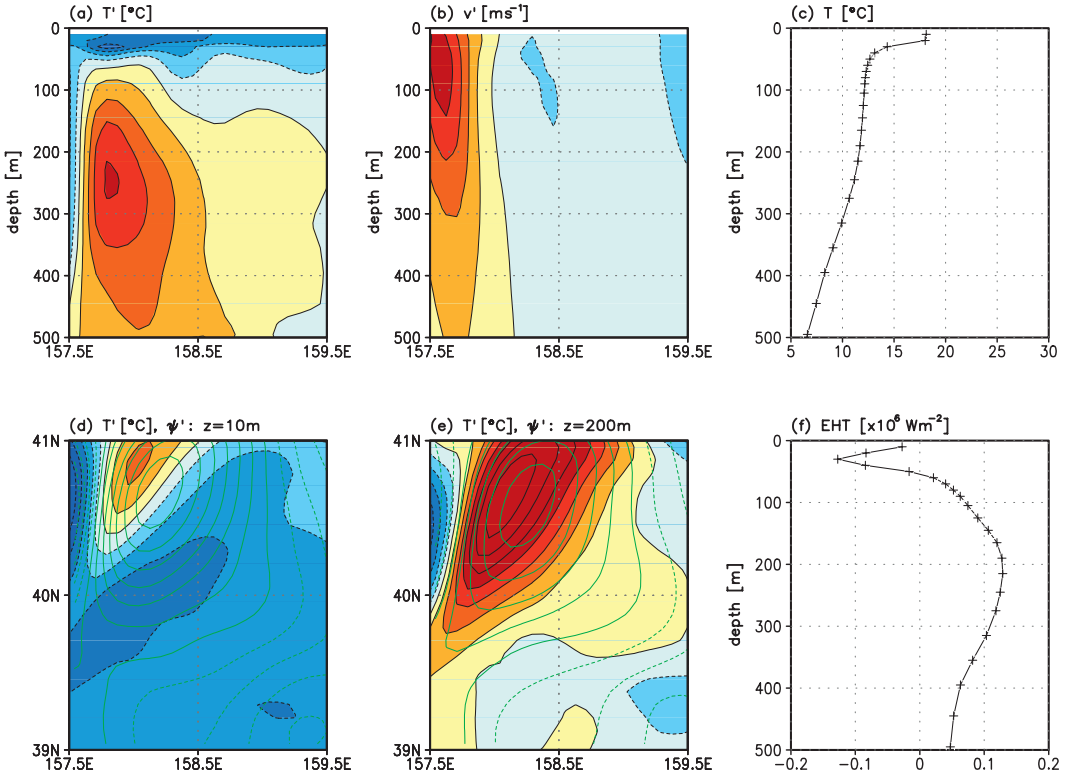

FIG. 9. As in Fig. 8, but in region 40NW (39°–41°N, 157.5°–159.5°E) on 6 Jul. Contour intervals are 0.5°C, 0.1 m s^{-1}, and 0.2×10^4 m^2 s^{-1} for T', v', and ψ'.

smaller and H_e larger in winter than in summer and fall, as shown in Figs. 4a and 4b. The annual mean value of $\partial\overline{T}/\partial y$ is very small at the surface but becomes large below the surface near $z = 100$ m, reflecting the temperature structure of the equatorial ocean associated with the NECC. Note that EHT is always directed toward the equator regardless of $\partial\overline{T}/\partial y$ in this region, implying the negative eddy diffusivity below $z = 200$ m, which was also suggested by Bryden and Brady (1989) from the analysis of observational data. It also leads to strong southward D-EHT, which is contrary to the northward D-EHT obtained by using Fickian diffusion (Stammer 1998).

The change of the sign of $\partial\overline{T}/\partial y$ with depth also appears in 10N. The positive value of $\partial\overline{T}/\partial y$ below the surface here is due to downwelling at the center of the subtropical gyre, as observed in Fig. 3b. This leads to the change of sign of EHT with depth and, consequently, leads to the negative H_e, as shown in Fig. 3a. Very small EHT in fall is attributed to small values of $\partial\overline{T}/\partial y$ and EKE.

In 40NW, EHT varies rapidly across the seasonal thermocline in summer, while it decreases gradually with depth in winter. Meanwhile, in 40NE, EHT disappears below the seasonal thermocline. It indicates that the decrease of H_e in the presence of a seasonal thermocline in the extratropical ocean is caused not only by the disappearance of EHT below the thermocline, as suggested by Qiu and Chen (2005), but also by the change of its sign.

Finally, the fact that EHT always persists up to a far greater depth below the mixed layer regardless of season in 40NW but disappears below the mixed layer in 40NE suggests that the annual mean H_e is much larger in 40NW than in 40NE. It implies that the annual mean value of H_e is larger in the region with larger H_k, as observed in Fig. 3.

e. *Effect of a seasonal thermocline on the structure of mesoscale eddies*

Figure 7 shows clearly that EHT is significantly modified in the presence of a seasonal thermocline. To clarify the process of how the seasonal thermocline affects EHT, we investigated the structure of mesoscale eddies across the seasonal thermocline. Figures 8–11 show the distributions of temperature and velocity anomalies in the vertical plane and in the horizontal plane above and below the thermocline ($z = 10$, 200 m), together with the vertical profiles of the mean temperature and EHT at three different locations corresponding to the cases of 4N,

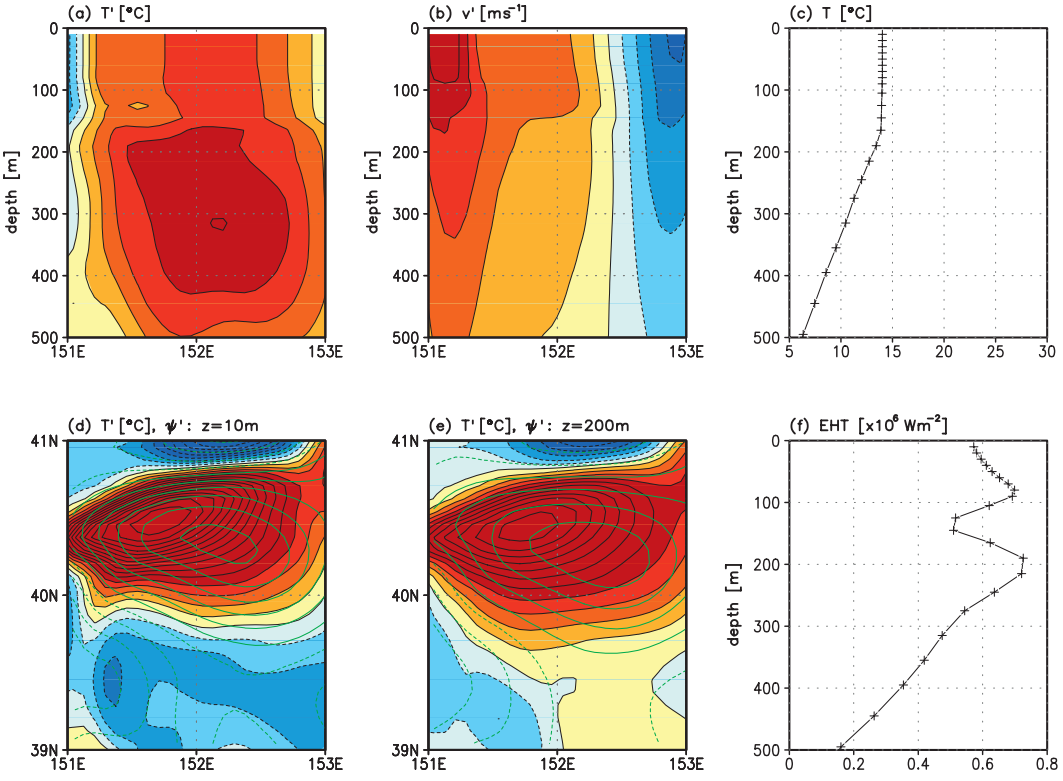

FIG. 10. As in Fig. 8, but in region 40NW (39°–41°N, 151°–153°E) on 30 Jan. Contour intervals are 0.5°C, 0.1 m s^{-1}, and 0.5 × 10^4 m^2 s^{-1} for T', v', and ψ'.

40NW, and 40NE. Only the winter case is considered for 4N and 40NE, but both the summer and winter cases are considered for 40NW.

The presence of mesoscale eddies, generated by baroclinic instability, induces a vertically coherent structure of the velocity and temperature field that is in quasigeostrophic balance. The cases of 4N and 40NW reveal that this temperature field is radically modified in the mixed layer by surface forcing such as heat flux, wind stress, and the turbulence generated by them, whereas the velocity field is not (Figs. 8 and 9). Because of this, the misalignment between the temperature and velocity field is enhanced remarkably, away from the geostrophic balance in the mixed layer, and EHT is substantially modified from that generated by baroclinic eddies. Furthermore, it is found that the misalignment between temperature and velocity is particularly strong near the seasonal thermocline, causing the strong deviation of EHT from the surrounding values. Note that the thermocline is much thicker in 4N ($z \sim 30$–150 m) than in 40NW ($z \sim 20$ m) because of the strong turbulence generation by subsurface shear in the tropical ocean (Noh and Lee 2008).

However, in 40NW winter, the modification of temperature in the mixed layer is not strong enough to destroy the eddy structure, probably because the heat flux from the sea surface is distributed over a much greater depth, while baroclinic instability is very strong (Fig. 10). As a result, EHT in the mixed layer is not as strongly modified in this case, although an abrupt change of EHT still appears near the thermocline, as in Figs. 8 and 9.

In the case of 40NE, mesoscale eddy activity is very weak, and there is virtually no EHT (Fig. 11). Note that contour intervals are one order smaller here than in Figs. 8–10. The EHT is mainly induced by the misalignment between temperature and velocity anomalies generated by surface forcing and, thus, is limited to the mixed layer.

The sensitivity of temperature and velocity anomalies to the seasonal thermocline can be clearly identified from the vertical profiles of the autocorrelation of temperature and velocity anomalies; that is, $\rho_T = \overline{T'(0)T'(z)}/\overline{T'(0)^2}$ and $\rho_v = \overline{v'(0)v'(z)}/\overline{v'(0)^2}$ (Fig. 12). It is found that ρ_v decreases gradually with depth unaffected by the presence of a seasonal thermocline. In 40NW, ρ_v decreases slowly with depth because of the presence of strong mesoscale eddies. On the other hand, ρ_T always decreases sharply across the seasonal thermocline. In the case of 40NW, ρ_T below the mixed layer remains positive, reflecting the presence of strong mesoscale eddies,

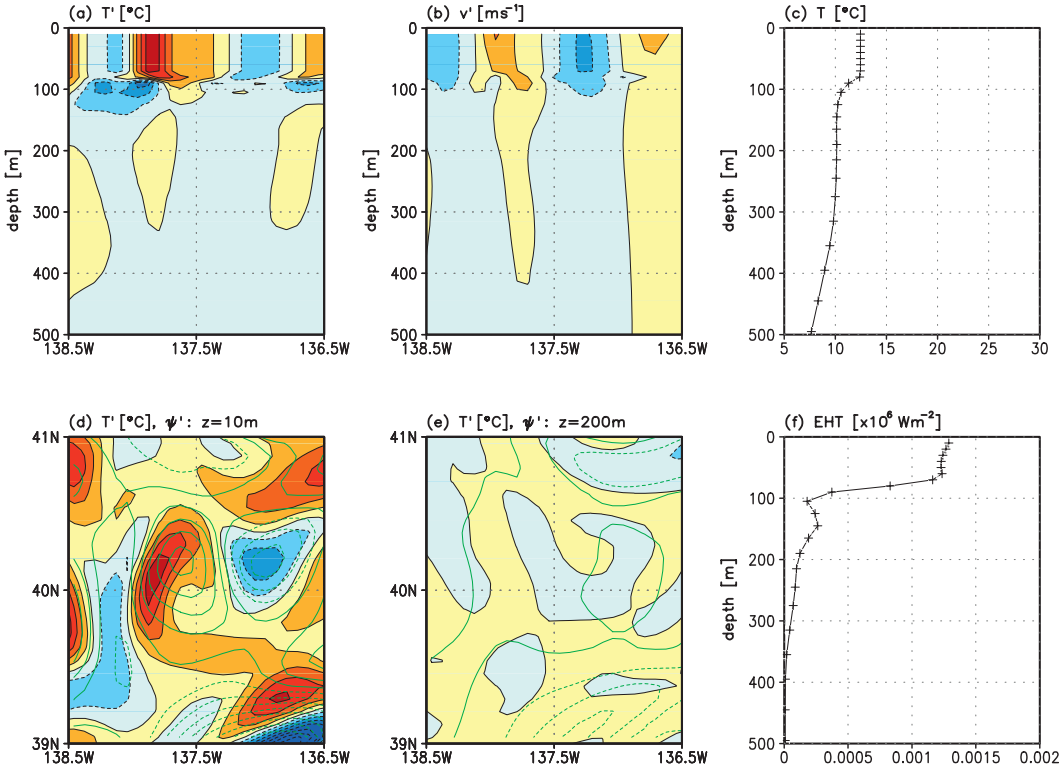

FIG. 11. As in Fig. 8, but in region 40NE (39°–41°N, 138.5°–136.5°W) on 12 Feb. Contour intervals are 0.05°C, 0.01 m s^{-1}, and 10^2 m^2 s^{-1} for T', v', and ψ'.

but its value is much smaller in summer than in winter, consistent with the fact that the vertical variation of EHT is strong in summer and weak in winter (Figs. 9 and 10).

The effect of a seasonal thermocline on the structure of mesoscale eddies illustrated above provides the clue to the relationship between H_e and H_d in the extratropical ocean, such as shown in Figs. 4–6. Examination of a large number of profiles of EHT reveals that the EHT in the Kuroshio Extension region shows strong vertical variation and often changes its sign with depth in summer (Figs. 7c and 9), whereas it decreases gradually with depth in winter (Figs. 7c and 10). On the other hand, in the eastern part of the extratropical Pacific Ocean, EHT occurs mainly within the mixed layer (Figs. 7d and 11). Both effects make D-EHT and H_e smaller in summer than in winter. In the tropical ocean, H_d is small throughout the year without noticeable seasonal variation, whereas EKE shows considerable seasonal variation (Figs. 7a,b). Therefore the seasonal variations of D-EHT and H_e are mainly controlled by EKE in the tropical ocean.

4. Conclusions

In the present paper, the vertical structure of EHT was investigated for the first time by analyzing an eddy-resolving OGCM covering the North Pacific with a horizontal resolution of 1/12°. Especially, the relationship between the effective depth of EHT H_e, the MLD H_d, and the penetration depth of EKE H_k was clarified. It was found that the annual mean value of H_e is generally proportional to H_k, but its seasonal variation is controlled by H_d in the extratropical ocean (>20°N).

Examination of vertical profiles revealed that the decrease of H_e in the presence of a seasonal thermocline in the extratropical ocean is caused by the disappearance of EHT below the thermocline in the region with weak EKE (e.g., the eastern extratropical ocean) or by the strong modification of EHT across the seasonal thermocline in the region with strong EKE (e.g., the Kuroshio Extension region). The strong modification of EHT across the seasonal thermocline was found to be attributed to the fact that the temperature field associated with mesoscale eddies is radically modified by surface forcing in the mixed layer, while the velocity field is not. In the tropical ocean, the seasonal variation of H_e is mainly controlled by H_k because the seasonal variation of H_d is insignificant compared to that of EKE.

The information on H_e obtained in this paper is expected to provide information for the estimation of

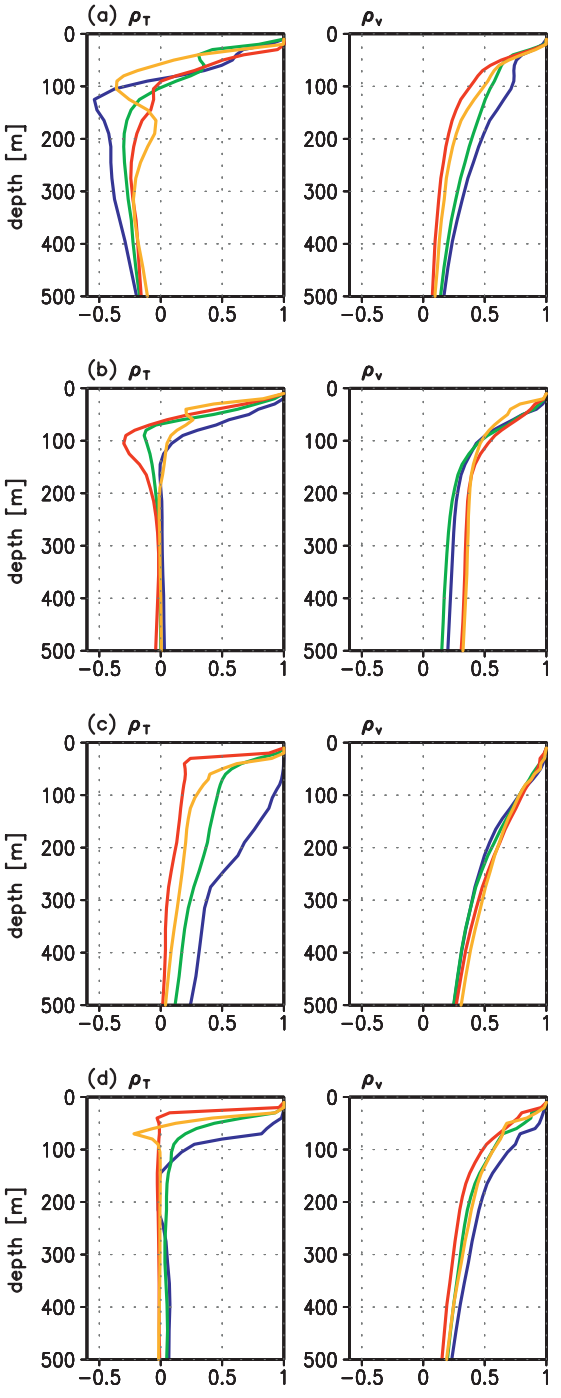

FIG. 12. Vertical profiles of the zonally averaged values of autocorrelations of temperature ρ_T and meridional velocity anomalies ρ_v in JFM: winter (blue), AMJ: spring (green), JAS: summer (red), and OND: fall (yellow) for (a) 4°N east (>170°W), (b) 10°N, (c) 40°N west (<170°W), and (d) 40°N east (>170°W).

D-EHT from satellite data. Furthermore, the effects of the mixed layer on the lateral mixing shown in the present paper can be applied to improve the lateral mixing scheme in the coarse-resolution OGCM, which currently concerns mainly the parameterization of baroclinic eddies (e.g., Killworth 1998).

Acknowledgments. This work was supported by the Korean Research Foundation Grant funded by the Korean Government (KRF-2008-313-C00944).

REFERENCES

Baturin, N. G., and P. P. Niiler, 1997: Effects of instability waves in the mixed layer of the equatorial Pacific. *J. Geophys. Res.,* **102,** 27 771–27 793.

Bower, A. S., and N. G. Hogg, 1996: Structure of the Gulf Stream and its recirculations at 55°W. *J. Phys. Oceanogr.,* **26,** 1002–1022.

Bryden, H. L., 1979: Poleward heat flux and conversion of available potential energy in Drake Passage. *J. Mar. Res.,* **37,** 1–22.

——, and R. A. Heath, 1985: Energetic eddies at the northern edge of the Antarctic Circumpolar Current in the southwest Pacific. *Prog. Oceanogr.,* **14,** 65–87.

——, and E. C. Brady, 1989: Eddy momentum and heat fluxes and their effects on the circulation of the equatorial Pacific Ocean. *J. Mar. Res.,* **47,** 55–79.

Cronin, M., and D. R. Watts, 1996: Eddy-mean flow interaction in the Gulf Stream at 68°W. Part I: Eddy energetics. *J. Phys. Oceanogr.,* **26,** 2107–2131.

Ducet, N., and P. Y. Le Traon, 2001: A comparison of surface eddy kinetic energy and Reynolds stresses in the Gulf Stream and the Kuroshio Current systems from merged TOPEX/Poseidon and ERX-1/2 altimetric data. *J. Geophys. Res.,* **106,** 16 603–16 622.

Gill, A. E., 1982: *Atmosphere–Ocean Dynamics*. Academic Press, 662 pp.

Hirose, N., H. Kawamura, H. J. Lee, and J. H. Yoon, 2007: Sequentual forecasting of the surface and subsurface conditions in the Japan Sea. *J. Oceanogr.,* **63,** 467–481.

Ishizaki, H., and T. Motoi, 1999: Reevaluation of the Takano–Oonishi scheme for momentum advection of bottom relief in ocean models. *J. Atmos. Oceanic Technol.,* **16,** 1994–2010.

Jayne, S. R., and J. Marotzke, 2002: The oceanic eddy heat transport. *J. Phys. Oceanogr.,* **32,** 3328–3345.

Kara, A. B., P. A. Rochford, and H. E. Hurlburt, 2003: Mixed layer depth variability over the global ocean. *J. Geophys. Res.,* **108,** 3079, doi:10.1029/2000JC000736.

Killworth, P., 1998: Eddy parameterization in large scale flow. *Ocean Modeling and Parameterization,* E. P. Chassignet and J. Verron, Eds., Kluwer Academic, 253–268.

Levitus, S., and T. P. Boyer, 1994: *Temperature*. Vol. 4, *World Ocean Atlas 1994,* NOAA Atlas NESDIS 4, 117 pp.

——, R. Burgett, and T. P. Boyer, 1994: *Salinity*. Vol. 3, *World Ocean Atlas 1994,* NOAA Atlas NESDIS 3, 99 pp.

Maltrud, M. E., and J. L. McClean, 2005: An eddy resolving global 1/10° ocean simulation. *Ocean Modell.,* **8,** 31–54.

Marshall, J., H. Jones, R. Karsten, and R. Wardle, 2002: Can eddies set ocean stratification? *J. Phys. Oceanogr.,* **32,** 26–38.

Meijers, A. J., N. L. Bindoff, and J. L. Roberts, 2007: On the total, mean, and eddy heat and freshwater transports in the Southern Hemisphere of a 1/8° × 1/8° global ocean model. *J. Phys. Oceanogr.,* **37,** 277–295.

Monterey, G., and S. Levitus, 1997: *Seasonal Variability of Mixed Layer Depth for the World Ocean,* NOAA Atlas NESDIS 14, 100 pp.

Noh, Y., and H. J. Kim, 1999: Simulations of temperature and turbulence structure of the oceanic boundary layer with the improved near-surface process. *J. Geophys. Res.,* **104,** 15 621–15 634.

——, and W. S. Lee, 2008: Mixed and mixing layer depths simulated by an OGCM. *J. Oceanogr.,* **64,** 217–225.

——, C. J. Jang, T. Yamagata, P. C. Chu, and C. H. Kim, 2002: Simulation of more realistic upper-ocean process from an OGCM with a new ocean mixed layer model. *J. Phys. Oceanogr.,* **32,** 1284–1307.

——, B. Y. Yim, S. H. You, J. H. Yoon, and B. Qiu, 2007: Seasonal variation of eddy kinetic energy of the North Pacific Subtropical Countercurrent simulated by an eddy-resolving OGCM. *Geophys. Res. Lett.,* **34,** L07601, doi:10.1029/2006GL029130.

Philander, S. G. H., and R. C. Pacanowski, 1986: The mass and heat budget in a model of the tropical Atlantic Ocean. *J. Geophys. Res.,* **91,** 14 212–14 220.

Qiao, L., and R. H. Weisberg, 1995: Tropical instability wave kinematics: Observations from the Tropical Instability Wave Experiment. *J. Geophys. Res.,* **100,** 8677–8693.

Qiu, B., 1999: Seasonal eddy field modulation of the North Pacific Subtropical Countercurrent: TOPEX/Poseidon observations and theory. *J. Phys. Oceanogr.,* **29,** 2471–2486.

——, and S. Chen, 2005: Eddy-induced heat transport in the subtropical North Pacific from Argo, TMI, and altimetry measurements. *J. Phys. Oceanogr.,* **35,** 458–473.

Roemmich, D., and J. Gilson, 2001: Eddy transport of heat and thermocline waters in the North Pacific: A key to interannual/decadal climate variability? *J. Phys. Oceanogr.,* **31,** 675–687.

Smith, R. D., M. E. Maltrud, F. O. Bryan, and M. W. Hecht, 2000: Numerical simulation of the North Atlantic Ocean at $^1/_{10}°$. *J. Phys. Oceanogr.,* **30,** 1532–1561.

Stammer, D., 1997: Global characteristics of ocean variability estimated from regional TOPEX/POSEIDON altimeter measurements. *J. Phys. Oceanogr.,* **27,** 1743–1769.

——, 1998: On eddy characteristics, eddy transports, and mean flow properties. *J. Phys. Oceanogr.,* **28,** 727–739.

——, C. Wunsch, and K. Ueyoshi, 2006: Temporal changes in ocean eddy transports. *J. Phys. Oceanogr.,* **36,** 543–550.

Volkov, D. L., T. Lee, and L. L. Fu, 2008: Eddy-induced meridional heat transport in the ocean. *Geophys. Res. Lett.,* **35,** L20601, doi:10.1029/2008GL035490.

Webb, D. J., B. A. de Cuevas, and C. S. Richimond, 1998: Improved advection scheme for ocean models. *J. Atmos. Oceanic Technol.,* **15,** 1171–1187.

Wunsch, C., 1999: Where do ocean eddy heat fluxes matter? *J. Geophys. Res.,* **104,** 13 235–13 249.

Wyrtki, K., and B. Kilonsky, 1984: Mean water and current structure during the Hawaii to Tahiti shuttle experiment. *J. Phys. Oceanogr.,* **14,** 242–254.

You, S. H., 2005: A numerical study of the Kuroshio System southwest of Japan. Ph.D. thesis, Kyushu University, 207 pp.